

Showcasing research from Prof. Zhongwei Chen's group at the University of Waterloo, Canada.

Structural and chemical synergistic encapsulation of polysulfides enables ultralong-life lithium-sulfur batteries

MnO₂ nanosheet-decorated hollow sulfur spheres have been designed and shown to efficiently entrap soluble lithium polysulfides from the synergistic effect of structural restriction and chemical encapsulation. This novel design strategy enables the achievement of an S cathode with ultralong life and high capacity, and paves new avenues in the practical application of high-performance Li-S batteries.

As featured in:



See Zhongwei Chen et al.,
Energy Environ. Sci., 2016, 9, 2533.



Cite this: *Energy Environ. Sci.*, 2016, 9, 2533

Received 20th January 2016,
Accepted 5th April 2016

DOI: 10.1039/c6ee00194g

www.rsc.org/ees

Structural and chemical synergistic encapsulation of polysulfides enables ultralong-life lithium–sulfur batteries†

Xiaolei Wang,‡ Ge Li,‡ Jingde Li, Yining Zhang, Ahn Wook, Aiping Yu and Zhongwei Chen*

An innovative design strategy for the structural and chemical synergistic encapsulation of polysulfides is proposed. Manganese dioxide nanosheet decorated hollow sulfur sphere nanocomposites are developed through a facile synthesis exhibiting ultralong cycling stability over 1500 cycles and high capacity for high-performance lithium–sulfur batteries.

Lithium–sulfur (Li–S) batteries have been regarded as one of the most promising high-energy power sources in a broad range of applications ranging from electric vehicles to large-scale grid energy storage.^{1–7} Li–S batteries deliver a theoretical energy of 2600 W h kg^{−1} that is an order of magnitude higher than that of the current lithium-ion batteries (LIBs), and utilize naturally abundant sulfur as the cathode material which significantly reduces the cost.^{8–11} The major challenge in the practical implementation of Li–S batteries resides in the dramatic capacity decay. The intermediate lithium polysulfides (Li_xS_n, 3 ≤ n ≤ 8) formed during cycling dissolve in the liquid electrolyte, migrate through the separator (Scheme 1a), and deposit on the Li metal anode, causing a “shuttle effect”. In addition, the utilization of the active material is strongly hampered by the intrinsic insulation of S and its discharge product Li₂S, leading to a low capacity and poor rate capability. Furthermore, the S cathode suffers from volume variation (~80%) during lithiation/de-lithiation, causing a loss of electrical contact and structural instability.^{12–16}

To address these challenges, an extensive research effort has been devoted to (i) the development of electrolyte additives to suppress the polysulfide shuttle and passivate the lithium–metal surface¹⁷ and (ii) the design of micro-/nano-structured cathodes to improve the conductivity and provide an efficient

Broader context

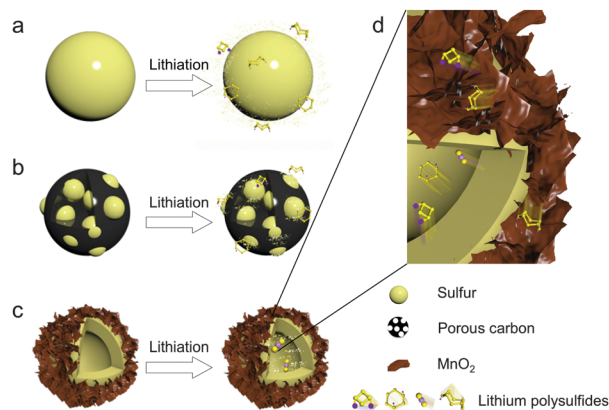
The fast depletion of fossil fuels and deterioration of the environment have led to an increasing demand for renewable energies and efficient energy storage technologies. Rechargeable lithium–sulfur (Li–S) batteries have been regarded as highly promising as they deliver an extremely high theoretical energy of 2600 W h kg^{−1} with low cost and toxicity by utilizing naturally abundant sulfur as the cathode material. The major challenge in the practical implementation of Li–S batteries resides in the dramatic capacity decay originated from the dissolution of intermediate lithium polysulfides into liquid electrolytes, and the loss of electrical contact and the structural instability due to the volume variation of sulfur during cycling. To address these issues, we report here for the first time a novel design strategy to efficiently entrap lithium polysulfides from the synergistic effect of structural restriction and chemical encapsulation using metal oxide-decorated hollow sulfur spheres. The hollow spheres with inner void space not only alleviate the volume expansion of S upon lithiation but also structurally restrict soluble lithium polysulfides within the spherical structure while the decorated metal oxide nanosheets with a large surface area chemically minimize polysulfide dissolution by forming strong bonds. Such a unique composite architecture enables the achievement of an S cathode with ultralong cyclability and high capacity for high-performance Li–S batteries.

polysulfide reservoir.^{18–23} The most common strategy for cathode design has mainly involved the encapsulation of sulfur within the conductive matrix, since Nazar’s pioneering concept of constraining S in ordered mesoporous carbon channels.²⁴ Other carbon materials (e.g. porous/hollow carbon,^{25–29} graphene/graphene oxides,^{30–32} and carbon nanotubes,^{33,34}), conductive polymers^{35,36} and non-carbon porous materials (e.g. mesoporous silica (SBA-15),³⁷ titania³⁸ and metal–organic frameworks³⁹) have been used to improve the cathode performance.^{40–42} Although improved cycling has been achieved, the weak interaction between Li_xS_n and these materials cannot provide efficient protection, thus these materials alone cannot serve as an ideal matrix (Scheme 1b). Low-level sulfur loading and complex preparation are also inevitable, and significantly limit the manufacturability of the S cathode. On the other hand, it has been

Department of Chemical Engineering, Waterloo Institute for Nanotechnology, Waterloo Institute for Sustainable Energy, University of Waterloo, Waterloo, Ontario N2L 3G1, Canada. E-mail: zhwen@uwaterloo.ca

† Electronic supplementary information (ESI) available: Detailed experimental methods and characterization are described. See DOI: 10.1039/c6ee00194g

‡ These authors contributed equally to this work.



Scheme 1 Schematic of the lithiation process in various S-based materials. (a) Bare S particles suffer from severe polysulfide dissolution. (b) Porous carbon materials provide structural restriction of S, the Li_xS_n dissolution and diffusion still occur. (c) The MnO_2 -decorated hollow S spheres provide both structural and chemical encapsulation of Li_xS_n . (d) The soluble Li_xS_n preferably diffuses within the hollow structure, or strongly anchors on MnO_2 nanosheets.

discovered that the polysulfides can be bonded to the host through either interactions or chemical reactions.¹⁴ To date, MnO_2 ,^{43,44} Ti_4O_7 ,^{45,46} Ti_2C ,⁴⁷ TiS_2 ,⁴⁸ N- or S-dopants^{49,50} and $\text{Co}(\text{OH})_2$ ⁵¹ have been reported with a relatively strong bonding effect with lithium polysulfides, and effectively entrap these species. However, the understanding of the interactions is limited to the polar/non-polar effect, and the detailed bonding mechanism at the molecular level is still unknown.^{14,44} Moreover, the preparation of these host-S composites is realized by either simple physical mixing or elaborate procedures, owing to the active nature of S.^{43,44} In this context, it is still highly demanded and is greatly challenging to design and develop S-based composites with structural and chemical dual-encapsulation of Li_xS_n for high-performance Li-S batteries.

Herein, we demonstrate an innovative strategy to efficiently entrap Li_xS_n through the synergistic effect of structural restriction and chemical encapsulation using metal oxide-decorated hollow sulfur spheres (Scheme 1c). The significance of this strategy lies in that we purposely design a material architecture with both structural and chemical encapsulation effects, and that the material architecture provides a prolonged cycling stability. MnO_2 is selected as a model and the MnO_2 nanosheet-decorated hollow S sphere (hollow S- MnO_2) nanocomposites are achieved through a facile synthesis. The nanocomposites with a unique structure possess several features that favor highly stable S electrodes (Scheme 1d): (i) the hollow spheres with inner void space not only alleviate the volume expansion of S on lithiation but also structurally restrict soluble Li_xS_n within the spherical structure; (ii) the decorated MnO_2 nanosheets with a large surface area efficiently and chemically minimize polysulfide dissolution by forming strong bonds; and (iii) the small dimensions of the hollow S- MnO_2 nanocomposites facilitate both ion and electron transport, leading to a better utilization of the S. This design presents a new strategy to prevent the loss of polysulfides *via* structural and chemical dual-encapsulation,

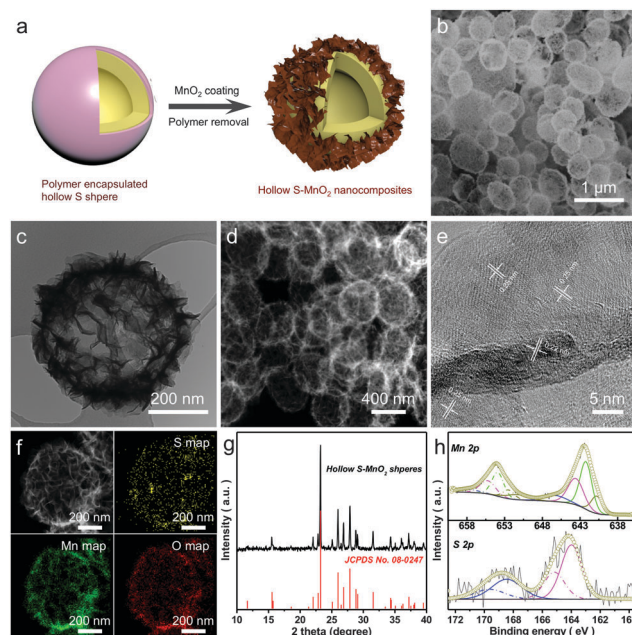


Fig. 1 (a) Schematic of the synthetic process of the hollow S- MnO_2 nanocomposites. (b) SEM, (c) TEM, and (d) dark field STEM images of the hollow S- MnO_2 nanocomposite spheres. (e) HRTEM image of MnO_2 nanosheets. (f) Dark field STEM image of a single nanocomposite sphere and corresponding EDS mapping on elements S, Mn and O. (g) XRD pattern of the nanocomposites. (h) XPS core-level spectra of Mn and S.

and can be extended to other metal oxides or metal hydroxides. The unique material architecture enables the construction of high-performance S cathodes with high capacity, high sulfur loading and extremely low capacity decay of only 0.028% per cycle over 1500 cycles at 0.5 C.

The hollow S- MnO_2 nanocomposites were experimentally realized as shown schematically in Fig. 1a. Nearly monodisperse, polyvinylpyrrolidone (PVP)-encapsulated hollow S spheres were prepared through a bottom-up approach reported previously.¹⁵ The reaction of potassium permanganate with PVP results in the formation of MnO_2 densely coated on the surface of hollow spheres, followed by the removal of extra PVP. Fig. 1b shows the typical scanning electron microscopy (SEM) image of the as-synthesized nanocomposites that exhibit a spherical morphology and a rough surface (Fig. S1, ESI[†]). The composite spheres possess a hollow structure with an average diameter of around 300 nm. The representative transmission electron microscopy (TEM) and high angle annular dark field (HAADF) scanning TEM (STEM) images (Fig. 1c and d) clearly reveal the hollow structure. The observed veil-like transparent nanosheets imply the formation of two-dimensional MnO_2 (Fig. S2, ESI[†]). High-resolution TEM images (Fig. 1e and Fig. S3, ESI[†]) indicate that the nanosheets are highly crystalline and can be indexed to birnessite δ - MnO_2 (Fig. S4, ESI[†]).⁴³ The composite structure is further determined by energy-dispersive X-ray spectroscopy (EDS) mapping (Fig. 1f), which reveals the presence of S, Mn and O elements. The homogeneous dispersion of S and the uniform distribution of Mn and O elements indicate the successful formation of hollow S spheres and the

decoration of MnO₂ nanosheets on the surface of S spheres, which agrees well with the TEM observation. The electron energy loss spectroscopy (EELS) spectrum confirms the existence of elements S, Mn and O, while the EELS mapping images (Fig. S5, ESI†) further confirm the MnO₂-decorated hollow S structure. Fig. 1g shows the X-ray diffraction (XRD) pattern of the nanocomposites, which can be indexed to the highly crystalline cubic sulfur (JCPDS No. 08-0247). According to thermogravimetric analysis (TGA, Fig. S6, ESI†), the S content is calculated to be ~75.5 wt%. Fig. 1h presents the X-ray photoelectron spectroscopy (XPS) analysis of the nanocomposites (Fig. S7, ESI†) where the highly resolved spectra of S 2p can be interpreted into two doublets. The peaks at 163.99 and 165.17 eV are mainly from pure S, while two peaks are observed at higher energies (168.45 and 169.63 eV) suggesting the existence of SO_x species from the covalently bonded S with MnO₂, which will be discussed later.^{52–54} Correspondingly, the Mn 2p peaks show an obvious shift to lower energy regions, suggesting an increased density of electron clouds from S.

Fig. 2a shows the typical cyclic voltammetric (CV) curves of the composite electrodes for the first 10 cycles at a sweep rate of 0.1 mV s⁻¹. Two cathodic peaks located at 2.27 and 2.02 V can be observed corresponding to the transformation of S to long-chain lithium polysulfides and the subsequent conversion of long-chain to short-chain polysulfides (Li₂S₂/Li₂S), respectively. Two overlapped anodic peaks are found at 2.48 and 2.56 V corresponding to the reverse conversion from polysulfides to S.²⁰ As expected, the nanocomposites show good stability during scanning, since the CV curves for subsequent cycles are highly similar in both shape and size. Typical galvanostatic profiles of the composite electrodes at 0.2 C (Fig. 2b) exhibit two discharging plateaus and one charging plateau, respectively, which is consistent with CV observation.^{12,13,55} The composite

electrode delivers a relatively low initial discharge capacity of 1043 mA h g⁻¹ due to the self-discharging. A charge capacity of 1240 mA h g⁻¹ is recovered corresponding to a Coulombic efficiency of 84.1%. The second cycle gives a discharge capacity of 1196 mA h g⁻¹ and a charge capacity of 1187 mA h g⁻¹, respectively, reaching ~72% of the theoretical capacity. The corresponding cycling performance is displayed in Fig. 2c. After the initial equilibrium cycles, the nanocomposites still possess a discharge capacity of 1072 mA h g⁻¹ after 200 cycles, which is even higher than its initial capacity and corresponds to 89.6% of its second capacity, indicating a long cycling stability with only 0.05% capacity loss per cycle. By comparison, the electrode using commercial S powders as the active material exhibits extremely low initial capacity and fast capacity decay (Fig. S8, ESI†). Although simply mixing commercial S powders with MnO₂ nanosheets results in improved cycling to some extent, the performance is not comparable to that of the nanocomposites (Fig. S9, ESI†). Note that the pure MnO₂ nanosheets obtained by the removal of S did not show significant contribution to the whole capacity under the same conditions (Fig. S10, ESI†).⁴³ As we mentioned above, the superior cycling stability is mainly ascribed to the MnO₂ nanosheet-decorated hollow structure, which favors the structural restriction of the polysulfides. On one hand, the polysulfides preferentially diffuse inwardly due to the steric hindrance. On the other hand, the hollow structure not only alleviates the volume change but also facilitates the ion-diffusion during cycling. The stable composite structure and fast electrode kinetics were further supported by the electrochemical impedance spectroscopy (EIS) measurements. A typical Nyquist plot of the composite electrode at various cycling status (Fig. 2d) reveals a low electrode series resistance (ESR) after activation cycling (Fig. S11, ESI†), which is well maintained after 50 cycles. It is also noteworthy that the areal capacity of the composite electrode is calculated to be 1.9–2.3 mA h cm⁻² based on the high S mass loading of 1.7–2.1 mg cm⁻², which is comparable or even higher than those of carbon-based composite electrodes.

To understand the superior cycling stability, the interaction between MnO₂ and Li_xS_n was investigated by X-ray photoelectron spectroscopy (XPS) analysis on the MnO₂/polysulfides composites. The MnO₂ nanosheets were obtained by dissolving S in CS₂ and then dispersed in dimethyl ether (DME). The polysulfides (mainly Li₂S₄ as the representative Li_xS_n species) were synthesized according to the literature^{43,56} and dissolved in 1,3-dioxolane (DOL) forming a transparent yellow solution. The addition of MnO₂ dispersion renders the Li₂S₄ solution colorless immediately and the MnO₂ precipitates shortly after (Fig. 3a), indicating the strong adsorption capability of MnO₂.

The Mn 2p_{3/2} spectrum of the composite exhibits a strong contribution from Mn⁴⁺ that appears as a characteristic multiplet with a maximum at 642.29 eV and other two satellite peaks at 643.7 and 646.49 eV. Compared to the pure MnO₂, the contribution from the Mn²⁺ ions significantly increases, indicated by the strong peak located at 640.87 eV (Fig. 3b).^{57,58} Obviously, MnO₂ is partially reduced. The reduction of Mn⁴⁺ to Mn²⁺ is accompanied by the oxidation of Li₂S₄, whose S 2p spectrum shows the bridging and terminal sulfur atoms in a 1:1 ratio.⁴³ In the

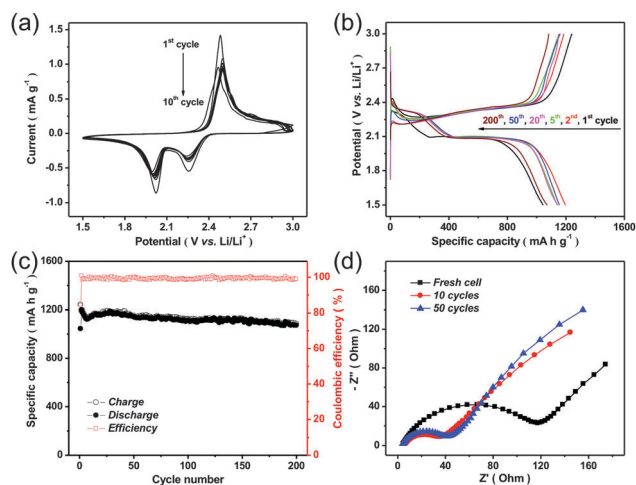


Fig. 2 (a) First ten cycle CV curves of the hollow S–MnO₂ nanocomposites at a sweeping rate of 0.1 mV s⁻¹ within 1.5–3.0 V versus Li/Li⁺. (b) Galvanostatic charge–discharge profiles at 0.2 C for various cycles. (c) Corresponding cycling performance and Coulombic efficiency for 200 cycles. (d) Nyquist plots of the hollow S–MnO₂ nanocomposite electrodes at different cycling statuses from 1 MHz to 10 mHz at room temperature.

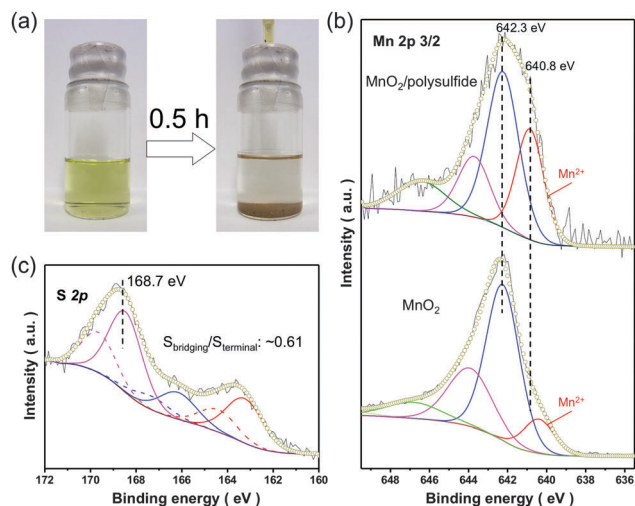


Fig. 3 (a) Digital picture of the fast encapsulation of lithium polysulfides by MnO_2 . (b) Comparison of XPS core-level spectra of element Mn in pure MnO_2 and MnO_2 /encapsulated lithium polysulfide composites. (c) Core-level spectra of element S in the MnO_2 /encapsulated polysulfide composites.

composites, the S 2p spectrum can be interpreted as three doublets (Fig. 3c). The two doublets located at 167.49/166.31 eV and 164.57/163.39 eV, with a splitting energy of 1.18 eV, are attributed to the bridging and terminal sulfur atoms. However, the ratio decreases to ~ 0.61 , owing to the significantly increased contribution from the peaks between 171 and 167 eV, suggesting the existence of S in higher valence states.⁵³ As we mentioned above, the significant amount of Mn^{2+} implies the chemical reactions occurring between MnO_2 and Li_xS_n , forming strong chemical bonds for Li_xS_n confinement. The two peaks from the S 2p spectrum located at 168.58 and 169.76 eV are mainly attributed to the SO_x species.⁵⁴

To further understand how the MnO_2 nanosheets adsorb Li_xS_n by forming strong chemical bonds, we analyze the composites using density functional theory (DFT) calculations. The interaction of various Li_xS_n species (including S_8 , Li_2S_8 , Li_2S_6 , Li_2S_4 , Li_2S_2 and Li_2S) with the $\delta\text{-MnO}_2$ nanosheet (100) surface anchoring support was investigated.^{14,59} The bonding energies (E_{bind}) of Li_xS_n species with MnO_2 were calculated as follows:

$$E_{\text{bind}}(\text{Li}_x\text{S}_n) = E(\text{Li}_x\text{S}_n/\text{MnO}_2) - E(\text{Li}_x\text{S}_n) - E(\text{MnO}_2) \quad (1)$$

A negative E_{bind} corresponds to a stable adsorbate/slab system and a favored interaction. Fig. 4a shows the geometries of the most stable adsorption configurations. The corresponding lithiation evolutions of binding energy are plotted in Fig. 4b. In the initial stage, the S_8 cluster is adsorbed on MnO_2 with a binding energy of -1.60 eV. The adsorption is mainly originated from the double interactions between the terminal S atoms from the opened S_8 ring and the surface O atoms from MnO_2 . Based on interatomic distances, the chemical bonds of $\text{S}=\text{O}$ have already formed. As the lithiation proceeds and the formation of Li_2S_8 occurs, the binding energy increases significantly to -4.68 eV, indicating the formation of strong chemical bonds. The Li_2S_8 adsorption configuration shows that the strong chemical bonding is originated from both $\text{S}=\text{O}$ and $\text{Li}-\text{O}$ chemical bonds. After that,

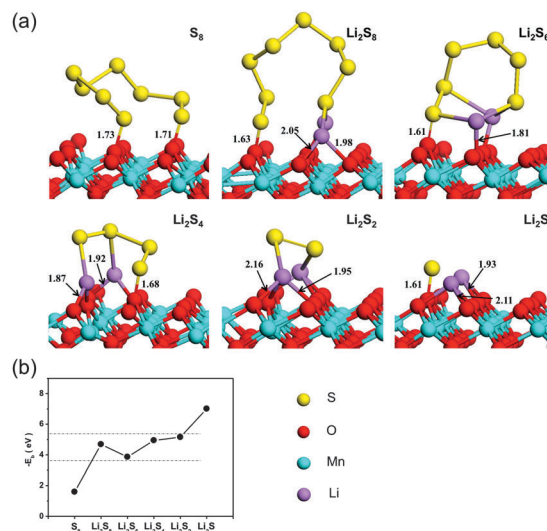


Fig. 4 (a) Optimized configurations for the binding of S, polysulfides and Li_2S to the MnO_2 . (b) Binding energies for lithium polysulfides at six different lithiation stages on MnO_2 .

the binding energy deviates in the range of -3.86 to -5.15 eV as lithiation progresses (Fig. 4b). When S is fully lithiated, Li_2S is not stable and eventually decomposes into Li and S atoms with the formation of $\text{S}=\text{O}$ and $\text{Li}-\text{O}$ bonds on the MnO_2 surface. Obviously, the interaction of S_8 with MnO_2 was relatively weak. By comparison, the interactions of the Li_xS_n species with the MnO_2 support are extremely strong, mainly attributed to the coexistence of $\text{Li}-\text{O}$ and $\text{S}=\text{O}$ bonds. Hirshfeld charge analysis clearly shows that electrons are transferred from the Li_xS_n species to the MnO_2 support, although the $\text{S}=\text{O}$ bond is also formed in the Li_2S_4 and Li_2S_6 cases (Fig. S12, ESI[†]). This result is consistent with the XPS analysis that MnO_2 efficiently anchors and prevents Li_xS_n from dissolving.

It is worth mentioning that the nanocomposites may not maintain the initial structure after repeated deep lithiation and the pulverization may not be avoidable. However, the fractured S and Li_xS_n are still entrapped within the MnO_2 networks built from unfolding and cross-linking elastic nanosheets (Fig. S13, ESI[†]). These MnO_2 networks through the whole electrode effectively preserve the electrode integrity, prevent the electrode from degrading and maintain the S accessibility. In particular, on the surface of the electrode, the interconnected nanosheets form a protection layer, preventing Li_xS_n from migrating to the anode side (Fig. S14, ESI[†]).

To investigate the efficiency of the structural and chemical synergistic effect, and the feasibility for practical application, long-term cycling was performed at 0.5 C. As shown in Fig. 5a, the nanocomposites exhibit an initial and second discharge capacity of 898 and 1110 mA h g^{-1} , respectively. After 1500 cycles, a discharge capacity of 644 mA h g^{-1} can still be obtained, corresponding to a capacity retention of 71.7% with high Coulombic efficiency. The capacity decay is calculated to be only 0.028% per cycle, which hits a new record among all reports with over 1000 cycles.^{15,43,60–64} The long-term cycling is further revealed at high current densities (Fig. S15, ESI[†]). A discharge capacity

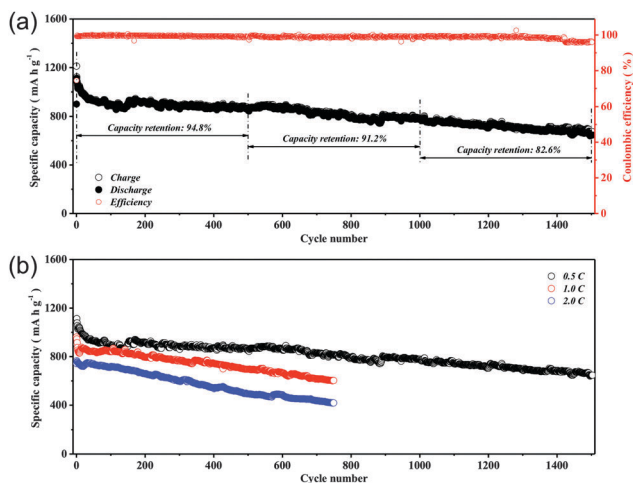


Fig. 5 (a) Long-term cycling stability of the composite electrode at 0.5 C-rate for 1500 cycles. (b) Comparison of the cycling stability of the composite electrodes at various C-rates.

retention of 62.6% and 56.1% after 750 cycles could also be achieved at 1.0 and 2.0 C, respectively (Fig. 5b). A few other composite architectures with a chemical confinement of Li_xS_n have been recently reported. For example, the nitrogen/sulfur-codoped graphene sponge can theoretically enhance the binding of Li_xS_n based on calculations,⁴⁹ while the hollow carbon fibers filled with MnO_2 composites can efficiently host sulfur.⁴⁴ However, these complicated preparation processes result in low yield and high cost, limiting their practical application. Obviously, our approach is facile, environmental benign and compatible with current large-scale production of electrode materials and electrode fabrication technology. With a low cost of starting materials (S, PVP and KMnO_4), the nanocomposites exhibit high manufacturability and can be readily scaled up at low cost.

Conclusions

In summary, we have demonstrated an innovative architectural design of hollow S spheres with decorated MnO_2 nanosheets, which provides the structural and chemical synergistic encapsulation of lithium polysulfides, as cathode materials for Li-S batteries with extremely long cycling stability. The nanocomposites exhibit lower capacity fading rate but higher or comparable sulfur fractions and loading than most porous carbon/S composites, which is mainly attributed to the efficient spatial restriction of the Li_xS_n and the strong interaction between MnO_2 and Li_xS_n enabling chemical encapsulation. This design concept paves new avenues in the practical application of the low-cost, high-energy, long-life Li-S batteries.

Acknowledgements

This work was financially supported by the Natural Sciences and Engineering Research Council of Canada (NSERC), the

University of Waterloo, and the Waterloo Institute for Nanotechnology. The authors acknowledge the Canadian Center for Electron Microscopy (CCEM) at McMaster University for TEM and HAADF-STEM support, and the Shared Hierarchical Academic Research Computing Network and Compute/Calcul Canada for the access to the facilities.

References

- P. G. Bruce, S. A. Freunberger, L. J. Hardwick and J.-M. Tarascon, *Nat. Mater.*, 2012, **11**, 19–29.
- N.-S. Choi, Z. Chen, S. A. Freunberger, X. Ji, Y.-K. Sun, K. Amine, G. Yushin, L. F. Nazar, J. Cho and P. G. Bruce, *Angew. Chem., Int. Ed.*, 2012, **51**, 9994–10024.
- L. F. Nazar, M. Cuisinier and Q. Pang, *MRS Bull.*, 2014, **39**, 436–442.
- J. M. Tarascon and M. Armand, *Nature*, 2001, **414**, 359–367.
- Z. Yang, J. Zhang, M. C. W. Kintner-Meyer, X. Lu, D. Choi, J. P. Lemmon and J. Liu, *Chem. Rev.*, 2011, **111**, 3577–3613.
- D. Bresser, S. Passerini and B. Scrosati, *Chem. Commun.*, 2013, **49**, 10545–10562.
- J. Liu, J.-G. Zhang, Z. Yang, J. P. Lemmon, C. Imhoff, G. L. Graff, L. Li, J. Hu, C. Wang, J. Xiao, G. Xia, V. V. Viswanathan, S. Baskaran, V. Sprenkle, X. Li, Y. Shao and B. Schwenzer, *Adv. Funct. Mater.*, 2013, **23**, 929–946.
- M. S. Whittingham, *Chem. Rev.*, 2004, **104**, 4271–4302.
- Y. Yang, G. Zheng and Y. Cui, *Chem. Soc. Rev.*, 2013, **42**, 3018–3032.
- J. B. Goodenough and Y. Kim, *Chem. Mater.*, 2010, **22**, 587–603.
- S. S. Zhang, *J. Power Sources*, 2013, **231**, 153–162.
- Y.-S. Su and A. Manthiram, *Nat. Commun.*, 2012, **3**, 1166.
- Y.-S. Su, Y. Fu, T. Cochell and A. Manthiram, *Nat. Commun.*, 2013, **4**, 2985.
- Q. Zhang, Y. Wang, Z. W. Seh, Z. Fu, R. Zhang and Y. Cui, *Nano Lett.*, 2015, **15**, 3780–3786.
- W. Li, G. Zheng, Y. Yang, Z. W. Seh, N. Liu and Y. Cui, *Proc. Natl. Acad. Sci. U. S. A.*, 2013, **110**, 7148–7153.
- S. Urbonaitė, T. Poux and P. Novák, *Adv. Energy Mater.*, 2015, **5**, DOI: 10.1002/aenm.201500118.
- S. Chen, F. Dai, M. L. Gordin, Z. Yu, Y. Gao, J. Song and D. Wang, *Angew. Chem., Int. Ed.*, 2016, **55**, 4231–4235.
- S. Meini, R. Elazari, A. Rosenman, A. Garsuch and D. Aurbach, *J. Phys. Chem. Lett.*, 2014, **5**, 915–918.
- W. Li, J. Hicks-Garner, J. Wang, J. Liu, A. F. Gross, E. Sherman, J. Graetz, J. J. Vajo and P. Liu, *Chem. Mater.*, 2014, **26**, 3403–3410.
- Y.-X. Yin, S. Xin, Y.-G. Guo and L.-J. Wan, *Angew. Chem., Int. Ed.*, 2013, **52**, 13186–13200.
- J. Scheers, S. Fantini and P. Johansson, *J. Power Sources*, 2014, **255**, 204–218.
- A. Rosenman, E. Markevich, G. Salitra, D. Aurbach, A. Garsuch and F. F. Chesneau, *Adv. Energy Mater.*, 2015, **5**, DOI: 10.1002/aenm.201500212.
- S. Evers and L. F. Nazar, *Acc. Chem. Res.*, 2013, **46**, 1135–1143.

- 24 X. Ji, K. T. Lee and L. F. Nazar, *Nat. Mater.*, 2009, **8**, 500–506.
- 25 G. He, S. Evers, X. Liang, M. Cuisinier, A. Garsuch and L. F. Nazar, *ACS Nano*, 2013, **7**, 10920–10930.
- 26 G. Zheng, Y. Yang, J. J. Cha, S. S. Hong and Y. Cui, *Nano Lett.*, 2011, **11**, 4462–4467.
- 27 C. Zhang, H. B. Wu, C. Yuan, Z. Guo and X. W. Lou, *Angew. Chem.*, 2012, **124**, 9730–9733.
- 28 N. Jayaprakash, J. Shen, S. S. Moganty, A. Corona and L. A. Archer, *Angew. Chem., Int. Ed.*, 2011, **50**, 5904–5908.
- 29 S. Rehman, S. Guo and Y. Hou, *Adv. Mater.*, 2016, DOI: 10.1002/adma.201506111.
- 30 H. Wang, Y. Yang, Y. Liang, J. T. Robinson, Y. Li, A. Jackson, Y. Cui and H. Dai, *Nano Lett.*, 2011, **11**, 2644–2647.
- 31 L. Ji, M. Rao, H. Zheng, L. Zhang, Y. Li, W. Duan, J. Guo, E. J. Cairns and Y. Zhang, *J. Am. Chem. Soc.*, 2011, **133**, 18522–18525.
- 32 S. Evers and L. F. Nazar, *Chem. Commun.*, 2012, **48**, 1233–1235.
- 33 G. Zhou, D.-W. Wang, F. Li, P.-X. Hou, L. Yin, C. Liu, G. Q. Lu, I. R. Gentle and H.-M. Cheng, *Energy Environ. Sci.*, 2012, **5**, 8901–8906.
- 34 J. Guo, Y. Xu and C. Wang, *Nano Lett.*, 2011, **11**, 4288–4294.
- 35 L. Xiao, Y. Cao, J. Xiao, B. Schwenzer, M. H. Engelhard, L. V. Saraf, Z. Nie, G. J. Exarhos and J. Liu, *J. Mater. Chem. A*, 2013, **1**, 9517–9526.
- 36 Y. Yang, G. Yu, J. J. Cha, H. Wu, M. Vosgueritchian, Y. Yao, Z. Bao and Y. Cui, *ACS Nano*, 2011, **5**, 9187–9193.
- 37 X. Ji, S. Evers, R. Black and L. F. Nazar, *Nat. Commun.*, 2011, **2**, 325.
- 38 S. Evers, T. Yim and L. F. Nazar, *J. Phys. Chem. C*, 2012, **116**, 19653–19658.
- 39 R. Demir-Cakan, M. Morcrette, F. Nouar, C. Davoisne, T. Devic, D. Gonbeau, R. Dominko, C. Serre, G. Férey and J.-M. Tarascon, *J. Am. Chem. Soc.*, 2011, **133**, 16154–16160.
- 40 X. Li, Y. Cao, W. Qi, L. V. Saraf, J. Xiao, Z. Nie, J. Mietek, J.-G. Zhang, B. Schwenzer and J. Liu, *J. Mater. Chem.*, 2011, **21**, 16603–16610.
- 41 D.-W. Wang, Q. Zeng, G. Zhou, L. Yin, F. Li, H.-M. Cheng, I. R. Gentle and G. Q. M. Lu, *J. Mater. Chem. A*, 2013, **1**, 9382–9394.
- 42 J. Guo, Z. Yang, Y. Yu, H. D. Abruña and L. A. Archer, *J. Am. Chem. Soc.*, 2013, **135**, 763–767.
- 43 X. Liang, C. Hart, Q. Pang, A. Garsuch, T. Weiss and L. F. Nazar, *Nat. Commun.*, 2015, **6**, 5682.
- 44 Z. Li, J. Zhang and X. W. Lou, *Angew. Chem., Int. Ed.*, 2015, **54**, 12886–12890.
- 45 Q. Pang, D. Kundu, M. Cuisinier and L. F. Nazar, *Nat. Commun.*, 2014, **5**, 4759.
- 46 X. Tao, J. Wang, Z. Ying, Q. Cai, G. Zheng, Y. Gan, H. Huang, Y. Xia, C. Liang, W. Zhang and Y. Cui, *Nano Lett.*, 2014, **14**, 5288–5294.
- 47 X. Liang, A. Garsuch and L. F. Nazar, *Angew. Chem., Int. Ed.*, 2015, **54**, 3907–3911.
- 48 Z. W. Seh, J. H. Yu, W. Li, P.-C. Hsu, H. Wang, Y. Sun, H. Yao, Q. Zhang and Y. Cui, *Nat. Commun.*, 2014, **5**, 5017.
- 49 G. Zhou, E. Paek, G. S. Hwang and A. Manthiram, *Nat. Commun.*, 2015, **6**, 7760.
- 50 J. Song, T. Xu, M. L. Gordin, P. Zhu, D. Lv, Y.-B. Jiang, Y. Chen, Y. Duan and D. Wang, *Adv. Funct. Mater.*, 2014, **24**, 1243–1250.
- 51 J. Zhang, H. Hu, Z. Li and X. W. Lou, *Angew. Chem., Int. Ed.*, 2016, **55**, 3982–3986.
- 52 L. Xiao, Y. Cao, J. Xiao, B. Schwenzer, M. H. Engelhard, L. V. Saraf, Z. Nie, G. J. Exarhos and J. Liu, *Adv. Mater.*, 2012, **24**, 1176–1181.
- 53 X. Wang, G. Li, M. H. Seo, F. M. Hassan, M. A. Hoque and Z. Chen, *Adv. Energy Mater.*, 2015, **5**, DOI: 10.1002/aenm.201501106.
- 54 X. Wang, G. Li, F. M. Hassan, J. Li, X. Fan, R. Batmaz, X. Xiao and Z. Chen, *Nano Energy*, 2015, **15**, 746–754.
- 55 L. Wang, D. Wang, F. Zhang and J. Jin, *Nano Lett.*, 2013, **13**, 4206–4211.
- 56 M. Cuisinier, P.-E. Cabelguen, S. Evers, G. He, M. Kolbeck, A. Garsuch, T. Bolin, M. Balasubramanian and L. F. Nazar, *J. Phys. Chem. Lett.*, 2013, **4**, 3227–3232.
- 57 B. Liu, X. Hu, H. Xu, W. Luo, Y. Sun and Y. Huang, *Sci. Rep.*, 2014, **4**, 4229.
- 58 K. Lei, X. Han, Y. Hu, X. Liu, L. Cong, F. Cheng and J. Chen, *Chem. Commun.*, 2015, **51**, 11599–11602.
- 59 C. Barchasz, F. Molton, C. Duboc, J.-C. Leprêtre, S. Patoux and F. Alloin, *Anal. Chem.*, 2012, **84**, 3973–3980.
- 60 G. Zhou, L. Li, C. Ma, S. Wang, Y. Shi, N. Koratkar, W. Ren, F. Li and H.-M. Cheng, *Nano Energy*, 2015, **11**, 356–365.
- 61 S. Moon, Y. H. Jung, W. K. Jung, D. S. Jung, J. W. Choi and D. K. Kim, *Adv. Mater.*, 2013, **25**, 6547–6553.
- 62 S. Lu, Y. Cheng, X. Wu and J. Liu, *Nano Lett.*, 2013, **13**, 2485–2489.
- 63 G. Li, J. Sun, W. Hou, S. Jiang, Y. Huang and J. Geng, *Nat. Commun.*, 2016, **7**, 10601.
- 64 L. F. Nazar and Q. Pang, *ACS Nano*, 2016, DOI: 10.1021/acsnano.5b07347.